ATP compartmentation in plastids and cytosol of *Arabidopsis thaliana* revealed by fluorescent protein sensing

Chia Pao Voon[a], Xiaoqian Guan[a], Yuzhe Sun[a], Abira Sahu[b], May Ngor Chan[a], Per Gardeström[c], Stephan Wagner[d,e], Philippe Fuchs[d,e], Thomas Nietzel[d,e], Wayne K. Versaw[b], Markus Schwarzländer[d,e], and Boon Leong Lim[a,f,1]

[a]School of Biological Sciences, The University of Hong Kong, Pokfulam, Hong Kong, China; [b]Department of Biology, Texas A&M University, College Station, TX 77843; [c]Umeå Plant Science Centre, Department of Plant Physiology, Umeå University, SE-901 87 Umeå, Sweden; [d]Institute of Crop Science and Resource Conservation, Rheinische Friedrich-Wilhelms-Universität Bonn, D-53113 Bonn, Germany; [e]Institute of Plant Biology and Biotechnology, Westfälische Wilhelms-Universität Münster, D-48143 Münster, Germany; and [f]State Key Laboratory of Agrobiotechnology, The Chinese University of Hong Kong, Shatin, Hong Kong, China

Edited by Bob B. Buchanan, University of California, Berkeley, CA, and approved September 26, 2018 (received for review June 27, 2017)

Matching ATP:NADPH provision and consumption in the chloroplast is a prerequisite for efficient photosynthesis. In terms of ATP:NADPH ratio, the amount of ATP generated from the linear electron flow does not meet the demand of the Calvin–Benson–Bassham (CBB) cycle. Several different mechanisms to increase ATP availability have evolved, including cyclic electron flow in higher plants and the direct import of mitochondrial-derived ATP in diatoms. By imaging a fluorescent ATP sensor protein expressed in living *Arabidopsis thaliana* seedlings, we found that $MgATP^{2-}$ concentrations were lower in the stroma of mature chloroplasts than in the cytosol, and exogenous ATP was able to enter chloroplasts isolated from 4- and 5-day-old seedlings, but not chloroplasts isolated from 10- or 20-day-old photosynthetic tissues. This observation is in line with the previous finding that the expression of chloroplast nucleotide transporters (NTTs) in *Arabidopsis* mesophyll is limited to very young seedlings. Employing a combination of photosynthetic and respiratory inhibitors with compartment-specific imaging of ATP, we corroborate the dependency of stromal ATP production on mitochondrial dissipation of photosynthetic reductant. Our data suggest that, during illumination, the provision and consumption of ATP:NADPH in chloroplasts can be balanced by exporting excess reductants rather than importing ATP from the cytosol.

ATP | chloroplasts | cytosol | mitochondria | photosynthesis

Chloroplasts and mitochondria are the major sites of ATP production in plant cells. Although chloroplasts generate ATP during photosynthesis, the amount of ATP produced relative to NADPH from linear electron flow (LEF) is theoretically insufficient for carbon fixation (ATP:NADPH, 1.28 vs. 1.5) (1, 2). The generation of additional ATP through alternative electron flow pathways, for example, cyclic electron flow (CEF), or through other mechanisms, is therefore necessary to support the Calvin–Benson–Bassham (CBB) cycle and photorespiration (2–4). In diatoms, mitochondria provide extra ATP to chloroplasts during periods of illumination to meet the ATP demand for carbon fixation (5). However, whether this mode of ATP supply is an efficient way to support the CBB cycle in higher plants has not been directly addressed.

Transport studies conducted with isolated chloroplasts suggest that plant chloroplasts can take up ATP from cytosol to support metabolic demands at night (6). It has also been suggested that chloroplasts may export ATP to the cytosol in the light or under stress conditions (7, 8). Illumination increases ATP/ADP ratios in both chloroplasts and the cytosol, particularly under conditions in which CO_2 is limiting (9, 10), but in vivo ATP dynamics in these two compartments have not been reported. Here, we analyzed intracellular compartmentation of ATP in live plants using a $MgATP^{2-}$-specific Förster resonance energy transfer (FRET)-based sensor protein, ATeam AT1.03-nD/nA (11–14). FRET ratio (FRET-derived acceptor emission/donor emission) of AT1.03-nD/nA increases with the concentration of $MgATP^{2-}$ (11). With a K_d of 50 μM for $MgATP^{2-}$ at 25 °C and pH 7.2 (15), and with a free Mg^{2+} concentration of 1–5 mM in leaves (16, 17), 95–99% of ATP is predicted to be complexed as $MgATP^{2-}$, which is also the biologically active form used by most enzymes. Cytosol- and plastid-targeted versions of the sensor were stably expressed in *Arabidopsis thaliana*, and $MgATP^{2-}$ concentrations were assessed for each cell compartment using confocal microscopy and ratiometric image analysis.

Results

Ratiometric Imaging of AT1.03-nD/nA in Plastids and Cytosol. The applicability of imaging AT1.03-nD/nA, hereafter AT1.03, to assess relative $MgATP^{2-}$ levels in intracellular compartments of *Arabidopsis thaliana* cells was recently demonstrated (13). The reported observations for chloroplasts and cytosol were confirmed and extended in this study. The emission spectrum for AT1.03 from 463 to 696 nm in 10-d-old seedlings was scanned with 458-nm excitation (*SI Appendix*, Fig. S1). Both cytosol- and plastid-localized AT1.03 showed characteristic emission peaks

Significance

By studying in vivo changes of ATP levels in the plastids and cytosol of *Arabidopsis thaliana* using a FRET-based ATP sensor, we show that the plastidic ATP concentrations in cotyledon, hypocotyl, and root of 10-day-old seedlings are significantly lower than the cytosolic concentrations. We show that chloroplasts consume ATP rapidly and the import of ATP into mature chloroplasts is impeded by the low density of NTT transporter. Hence, unlike in diatoms, where ATP is imported into chloroplasts to support the Calvin–Benson–Bassham (CBB) cycle, mature chloroplasts of *Arabidopsis* do not balance the ATP:NADPH ratio by importing ATP from the cytosol. Rather, chloroplasts can export surplus reducing equivalents, which can be used by the mitochondria to supply ATP to the cytosol.

Author contributions: C.P.V., P.G., W.K.V., M.S., and B.L.L. designed research; C.P.V., X.G., A.S., M.N.C., S.W., P.F., and T.N. performed research; C.P.V., Y.S., and A.S. analyzed data; and C.P.V. and B.L.L. wrote the paper.

The authors declare no conflict of interest.

This article is a PNAS Direct Submission.

[1]To whom correspondence should be addressed. Email: bllim@hku.hk.

This article contains supporting information online at www.pnas.org/lookup/suppl/doi:10.1073/pnas.1711497115/-/DCSupplemental.

Published online October 23, 2018.

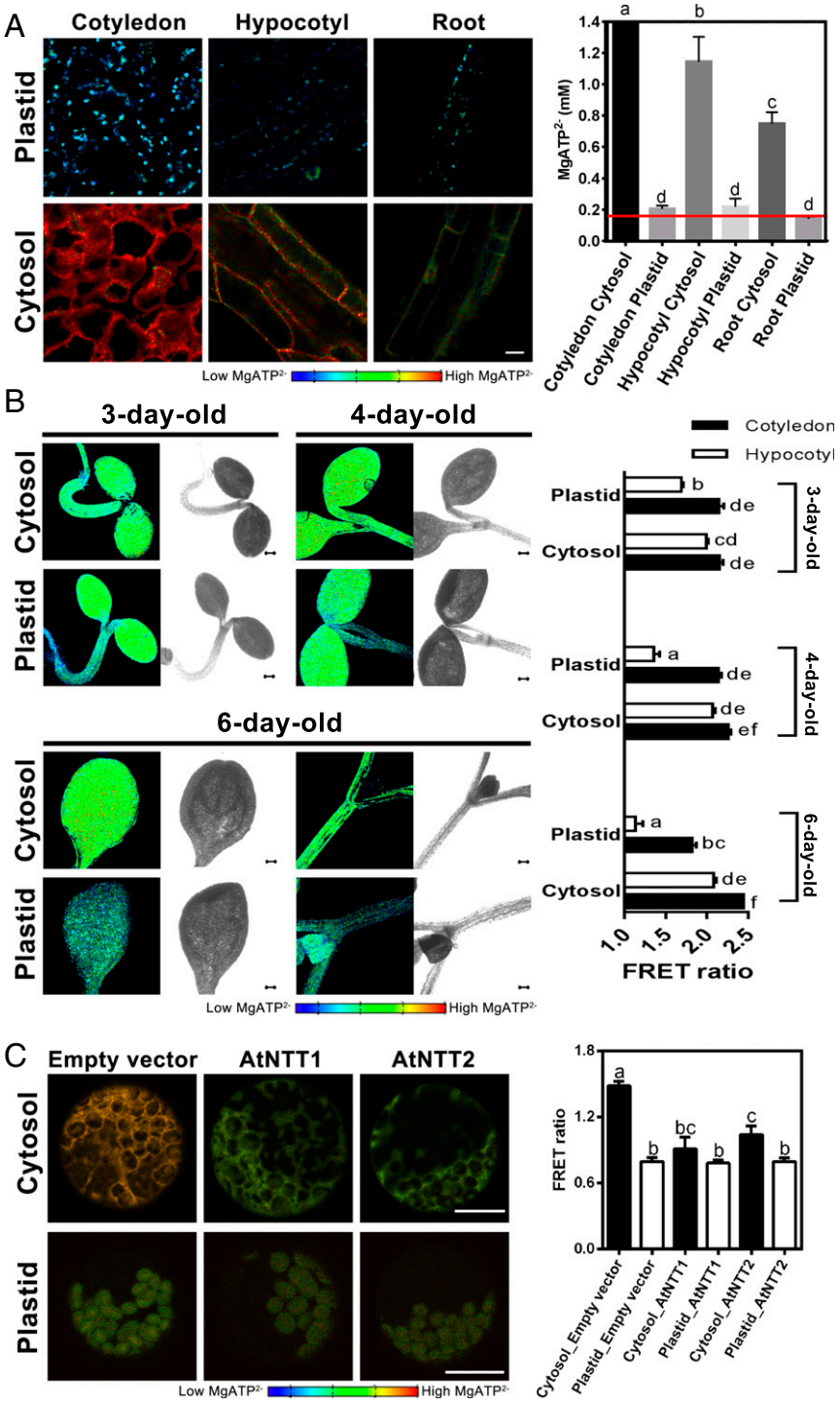

Fig. 1. Cytosolic and plastidic $MgATP^{2-}$ levels in different plant tissues. (*A*) Apparent cytosolic and plastidic $MgATP^{2-}$ concentrations in cotyledon, hypocotyl, and root cells of 10-d-old *Arabidopsis* seedlings estimated with the fluorescent biosensor AT1.03-nD/nA (n = 8–10 plants; mean ± SEM). Groups with significant difference by one-way ANOVA with post hoc Tukey HSD test ($P < 0.05$) are indicated by different letters. The maximal $MgATP^{2-}$ that can be reported by AT1.03-nD/nA is 1.4 mM. The red line indicates the lower detection limit of AT1.03-nD/nA (0.16 mM). Images show representative false color illustrations of the FRET ratios. (Scale bar: 20 μm.) (*B*) FRET ratios of cytosolic (C-) and plastidic (TKTP-) AT1.03-nD/nA in 3-, 4-, and 6-d-old *Arabidopsis* seedlings. Images show representative false color illustrations of the FRET ratios. (Scale bar: 200 μm.) FRET ratios of the plastidic and cytosolic sensors of both tissues of each day were compared (n = 6 plants; mean ± SEM), and groups with significant difference by one-way ANOVA with post hoc Tukey HSD test ($P < 0.05$) are indicated by different letters. (*C*) Protoplasts isolated from 4-wk-old *Arabidopsis* leaves expressing C-AT1.03-nD/nA and TKTP-AT1.03-nD/nA were transfected with empty vector (pENTR-35S) or vectors expressing AtNTT1 (At1g80300) and AtNTT2 (At1g15500). FRET ratios (n > 11 protoplasts; mean ± SEM) were compared, and groups with significant difference by one-way ANOVA with post hoc Tukey HSD test ($P < 0.05$) are indicated by different letters. (Scale bar: 20 μm.)

for mseCFP and cp173Venus (483 and 521–531 nm, respectively), whereas background fluorescence in control seedlings was negligible in this spectral region and was apparent only in the region of chlorophyll fluorescence (>630 nm). These data showed that chlorophyll fluorescence does not interfere with the ratiometric measurements of AT1.03.

An in situ calibration of the AT1.03 sensor in live seedlings was not possible because no ionophore for ATP was available and cell permeabilization treatments are not applicable for organelles. Therefore, to estimate concentrations of $MgATP^{2-}$ in cytosol and plastid stroma of plant cells, we performed in vitro calibration of FRET ratio (sensitized FRET/donor mseCFP emission) for the AT1.03 sensor using the same imaging parameters applied to live plants (*SI Appendix*, Fig. S2). From this calibration, we set conservative limits (0.16–1.4 mM) for the estimation of in vivo $MgATP^{2-}$ concentration. Correction factors used to calculate sensitized FRET from raw FRET emission values were empirically determined and applied for each tissue and cell compartment we examined (*SI Appendix*, Fig. S3) (18). These corrections accounted for donor bleedthrough and acceptor cross-excitation in each compartment as well as differences in local environments. As for any sensor calibration, the accuracy of estimates for in vivo ligand concentrations depends on the assumption that the sensor behaves similarly in vitro and in vivo. For the AT1.03 sensor, this assumption is supported by several observations. First, the sensor was insensitive to physiological concentrations of multiple cellular solutes, suggesting little or no nonspecific effects (*SI Appendix*, Fig. S4). Second, estimates of cytosolic and stromal ATP concentrations based on the in vitro AT1.03 calibration were consistent with values reported/inferred in previous studies (19, 20). Finally, illumination and metabolic inhibitors expected to alter $MgATP^{2-}$ concentration yielded changes in FRET ratio consistent with their modes of action (see below). Although it remains possible that our calibration results in consistent underestimates or overestimates of $MgATP^{2-}$ concentrations in vivo, the relative differences we observed between cell compartments and in response to metabolic inhibitors would remain valid.

$MgATP^{2-}$ Concentration in Plastid Stroma Is Lower than in Cytosol in 10-d-Old Cotyledon, Hypocotyl, and Root. $MgATP^{2-}$ concentrations were lower in plastid stroma in the cotyledon, hypocotyl, and root of 10-d-old seedlings than in the cytosol (Fig. 1*A*). This difference was also reflected in the in vivo spectra (*SI Appendix*, Fig. S1), where the mseCFP peak was lower for the cytosolic sensor than for the plastid sensor, while the relative intensities were reversed for the cp173Venus peak (*SI Appendix*, Fig. S1*B*). The cotyledon cytosol showed the highest $MgATP^{2-}$ concentration, which exceeded the maximum detection limit (>1.4 mM), whereas lower concentrations were detected in the hypocotyl (1.15 ± 0.39 mM) and root (0.75 ± 0.16 mM) cytosol (Fig. 1). These values are in the same range to that (0.40 ± 0.05 mM) determined by NMR for cytosolic $MgATP^{2-}$ in cultured, heterotrophic sycamore (*Acer pseudoplatanus* L.) cells (19). In 10-d-old seedlings, plastids in cotyledon, hypocotyl, and root showed low $MgATP^{2-}$ concentrations (0.16–0.21 mM) (Fig. 1*A*). Only plastids in the cotyledons of very young seedlings contained stromal $MgATP^{2-}$ levels as high as that of the cytosol (Fig. 1*B*), consistent with recent observations (13). The FRET ratios of cytosolic sensor and the plastid sensor are similar in the cotyledon of 3- and 4-d-old seedings, but the FRET ratio of the plastid sensor started to drop in the 6-d-old seedlings (Fig. 1*B*). Over the following days, stromal $MgATP^{2-}$ decreased to a similarly low level as in the hypocotyl and roots in 10-d-old seedlings (Fig. 1*A*). The difference between cytosolic and stromal $MgATP^{2-}$ concentrations was also observed in mesophyll protoplasts from 4-wk-old leaves (Fig. 1*C*).

Mature Chloroplasts Do Not Import ATP as Efficiently as Young Chloroplasts. Nonphotosynthetic plastids rely on the import of ATP from the cytosol to fuel biosynthetic processes in the stroma. It has been suggested that the nucleotide transporters (NTTs) that mediate this import also function in chloroplasts, despite restriction of their expression to heterotrophic tissues (21, 22). To examine whether transport capacity is limiting for the allocation of $MgATP^{2-}$ between cytosol and chloroplast stroma, we transiently expressed each of the *Arabidopsis* NTTs, AtNTT1 (At1g80300) and AtNTT2 (At1g15500), in mesophyll protoplasts (22). In both cases, we detected a reduction in cytosolic $MgATP^{2-}$ concentrations (Fig. 1*C*), which suggests that increasing the capacity for nucleotide entry into the chloroplast creates an additional intracellular ATP sink. We did not detect changes in stromal $MgATP^{2-}$, which may be due to its metabolic depletion after an overnight incubation. Consistently, addition of exogenous $MgATP^{2-}$ to isolated chloroplasts from 4- and 5-d-old AT1.03 seedlings increased the FRET ratios of the stromal sensor, but not in chloroplasts isolated from 10-d-old cotyledons or 20-d-old true leaves (Fig. 2*A*). The integrity of chloroplasts was verified by SYTOX orange nucleic acid staining (Fig. 2*B*). Increases in FRET ratio were observed in leaky 10-d-old chloroplasts, suggesting that the AT1.03 sensor was functional in mature chloroplasts. These results indicate that the ATP transport capacity of *Arabidopsis* chloroplasts decreases during early seedling development.

Chloroplasts Consume Stromal $MgATP^{2-}$ Rapidly. Illumination increased the concentration of $MgATP^{2-}$ in the stroma of chloroplasts in 10-d-old cotyledon tissues, but not in nongreen root plastids, consistent with ATP synthesis by the photosynthetic light reactions (Fig. 3*A*). A rapid increase was observed in the initial 30 s of illumination followed by a slower increase, suggesting the subsequent activation of ATP-consuming activities, such as the CBB cycle (Fig. 3*A*). The stromal $MgATP^{2-}$ concentration decreased rapidly to very low levels after the onset of darkness, indicating persisting and rapid ATP consumption (Fig. 3*A*). No change in FRET ratio was detected when the experiments were conducted with lines expressing a closely related FRET construct that cannot bind ATP species (cpFLIPPi-null) (*SI Appendix*, Fig. S5).

The Activity of Mitochondrial Respiratory Chain Is Stimulated by Photosynthesis. Illumination also caused an increase in the pH of the mitochondrial matrix (Fig. 3*B*), and the pH returned to the previous state within 30 s after illumination was terminated. In the presence of inhibitors of mitochondrial respiratory metabolism [rotenone, thenoyltrifluoroacetone (TTFA), antimycin A, and oligomycin], the change in pH induced by illumination was eliminated, pointing to proton pumping activity by the mitochondrial electron tranport chain (ETC) as the cause of the pH changes. The light-induced pH change was also eliminated by 3-(3,4-dichlorophenyl)-1,1-dimethylurea (DCMU), an inhibitor of photosynthesis, indicating that photosynthesis was ultimately responsible for the light-induced change in the matrix pH.

The Mitochondrion Is a Major Source of Cytosolic ATP. Metabolic inhibitors were further used to identify the source of ATP in the cytosol in the absence of illumination. The suppression of mitochondrial complex I (rotenone), complex II (TTFA), complex III (antimycin A), and complex V (oligomycin) decreased the $MgATP^{2-}$ concentration in the cytosol, whereas photosynthetic inhibitors DCMU and 2,5-dibromo-6-isopropyl-3-methyl-1,4-benzoquinone (DBMIB), and a mitochondrial alternative oxidase (AOX) inhibitor [salicylhydroxamic acid (SHAM)], did not affect the cytosolic concentration of $MgATP^{2-}$ (Fig. 4*A*), suggesting that the mitochondrion is the major supplier of ATP to the cytosol in the dark. No change in FRET ratio was detected

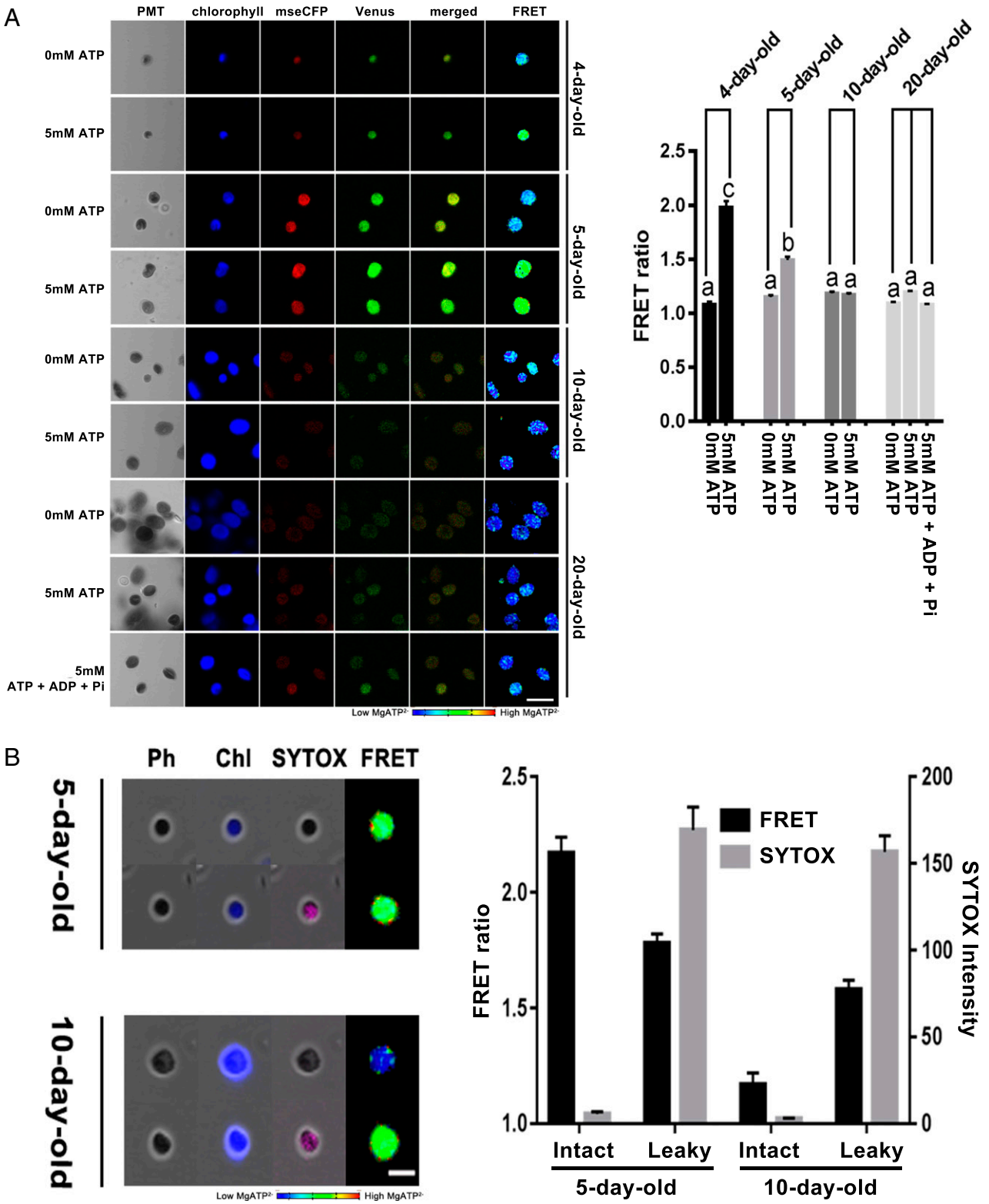

Fig. 2. Incubation of chloroplasts expressing TKTP-AT1.03-nD/nA with exogenous ATP. (*A*) Chloroplasts were isolated from 4-, 5-, and 10-d-old seedlings, and 20-d-old leaves. CLSM images of chlorophyll fluorescence (blue), mseCFP (red), cp173Venus (green), merged mseCFP (red), and cp173Venus (green) channels, and FRET ratios (FRET) of chloroplasts incubated in a buffer containing 5 mM $MgCl_2$ with 0 mM ATP, 5 mM ATP, or 5 mM ATP/ADP/Pi. (Scale bar: 10 μm.) FRET ratios (mean ± SEM) of chloroplasts from each group (n = 59, 34, 146, 203, 517, 706, 513, 954, and 30, respectively) are displayed in a graph. (*B*) Leaky chloroplasts were stained with SYTOX orange. CLSM images of phase contrast (Ph), phase contrast with chlorophyll fluorescence (Chl), phase contrast with SYTOX orange fluorescence (SYTOX), and FRET ratios (FRET) of chloroplasts are shown. (Scale bar: 5 μm.) FRET ratios and the corresponding SYTOX orange intensities (mean ± SEM) of chloroplasts (n = 32–154) are displayed in the graph. The SYTOX orange signals were significantly different between intact and leaky chloroplasts by one-way ANOVA with post hoc Tukey HSD test ($P < 0.001$). Lower FRET ratio is expected in the chloroplasts with SYTOX orange stain as the stain absorbs the FRET emission at 526–545 nm. Groups with significant difference in terms of FRET ratios by one-way ANOVA with post hoc Tukey HSD test ($P < 0.01$) are indicated by different letters.

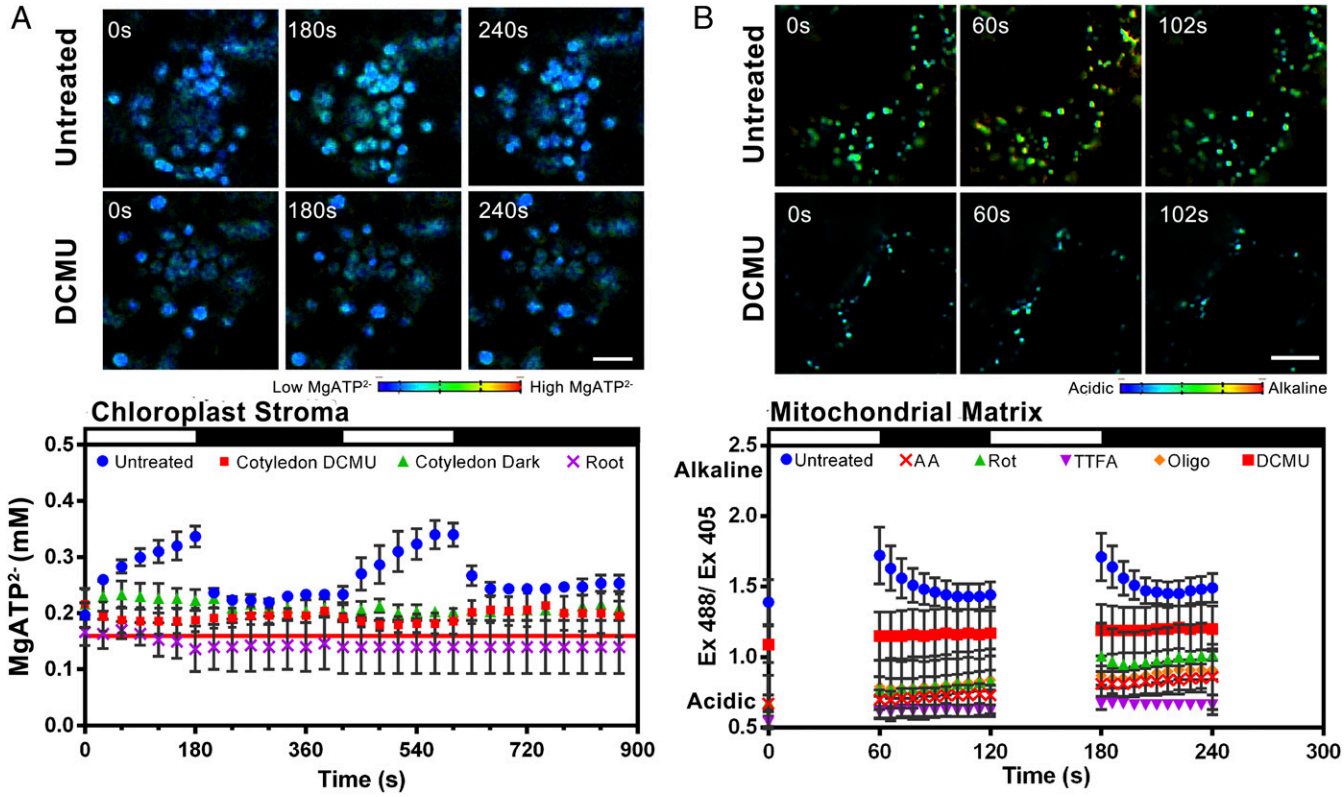

Fig. 3. Light responses of organellar $MgATP^{2-}$ and pH sensors. (*A*) The change of stromal $MgATP^{2-}$ concentrations in cotyledon and root in response to illumination. 10-d-old seedlings stably expressing the individual protein sensors were illuminated periodically at 296 $\mu mol \cdot m^{-2} \cdot s^{-1}$ or recorded in the dark where indicated by white or black boxes, respectively. Representative false color representation of the FRET ratio of stroma AT1.03-nD/nA in the presence or absence of the photosynthesis inhibitor DCMU before illumination (0 s), at the end of illumination (180 s), and shortly after illumination (240 s) are shown. The red line indicates the lower detection limit of AT1.03-nD/nA (0.16 mM). Values lower than the line are out of the detection limit. [Scale bar (all panels): 20 μm.] (*B*) The change of Ex_{488}/Ex_{405} ratio (pH) of mitochondrial matrix cpYFP in illuminated cotyledon in the presence of different inhibitors [AA, antimycin A; DCMU, 3-(3,4-dichlorophenyl)-1,1-dimethylurea; Oligo, oligomycin; Rot, rotenone; or TTFA, thenoyltrifluoroacetone] (n = 3; mean ± SEM). Representative false color images of the Ex_{488}/Ex_{405} ratios of cotyledons treated with DCMU are shown at different illumination conditions. [Scale bar (all panels): 20 μm.]

when the experiments were conducted with the ATP-insensitive cpFLIPPi-null sensor (*SI Appendix*, Fig. S5), suggesting that the changes observed with AT1.03 reflect altered $MgATP^{2-}$ concentrations (Fig. 4*A*). The inhibition of mitochondrial ATP synthase by oligomycin drained the cytosolic $MgATP^{2-}$ pool beyond the sensitivity limit of the sensor (<0.16 mM), whereas blocking the cytochrome *c* pathway at complex III by antimycin A had a less severe impact on cytosolic $MgATP^{2-}$ (0.23 ± 0.02 mM) (Fig. 4*A*). The suppression of AOX with SHAM did not affect the cytosolic $MgATP^{2-}$ concentration, confirming that AOX does not contribute to mitochondrial ATP production in the dark in the presence of an active cytochrome *c* pathway (Fig. 4*A*). Inhibition of either complex I or complex II, which feed electrons into the ETC by oxidizing NADH and succinate, respectively, only partially reduced cytosolic $MgATP^{2-}$ concentrations to 0.94 ± 0.13 and 0.75 ± 0.08 mM, respectively (Fig. 4*A*). Complex I can be bypassed by rotenone-insensitive, non–proton-pumping, type II NAD(P)H dehydrogenase activities in the mitochondrial inner membrane facing either the intermembrane space or matrix side, that is, NDex or NDin, respectively (23).

We then examined how illumination affected cytosolic $MgATP^{2-}$ concentration. Since cytosolic $MgATP^{2-}$ concentration in the cotyledon exceeded the maximum detection range of AT1.03 (>1.4 mM), we used rotenone to lower the initial steady-state concentration to 0.9 ± 0.12 mM. Illumination caused a rapid increase in cytosolic $MgATP^{2-}$ concentration, suggesting that ATP was delivered to or produced in the cytosol. Although we detected no chloroplast ATP transport at this developmental stage (Fig. 2), the application of DCMU abolished the light-dependent increase in cytosolic $MgATP^{2-}$ (Fig. 4*B*). This implies that photosynthesis is a driver of this process. In line with our interpretation, mitochondrial ETC activity was stimulated by illumination (Fig. 3*B*). We then examined whether cytosolic ATP can be enhanced by illumination when mitochondria were not able to synthesize ATP. Oligomycin treatment reduced the cytosolic ATP level below the lower detection limit (Fig. 4*C*). However, illumination caused a small increase in cytosolic $MgATP^{2-}$ (Fig. 4*C*). This increase was inhibited by an additional DCMU treatment. Assuming that oligomycin treatment resulted in complete inhibition of complex V, then the light-driven increase in cytosolic $MgATP^{2-}$ observed in the absence of DCMU (Fig. 4*C*) may be due to export of 3C compounds from chloroplasts to cytosol followed by their turnover through glycolysis and ATP production by substrate-level phosphorylation.

The Role of Mitochondria in Photosynthesis. To identify the mechanisms by which the mitochondrial ETC affects photosynthetic ATP production, changes in stromal $MgATP^{2-}$ concentration induced by illumination were monitored in seedlings that were treated with various mitochondrial inhibitors (Fig. 5*A* and *SI Appendix*, Fig. S6). Although the electron transport rate (ETR) and oxygen evolution rate were slightly decreased by rotenone (Fig. 5*B* and *SI Appendix*, Fig. S7, respectively), inhibition of complex I did not affect the change in chloroplast $MgATP^{2-}$ concentration upon illumination, suggesting that a partially active mitochondrial ETC [e.g., type II NAD(P)H dehydrogenases] was

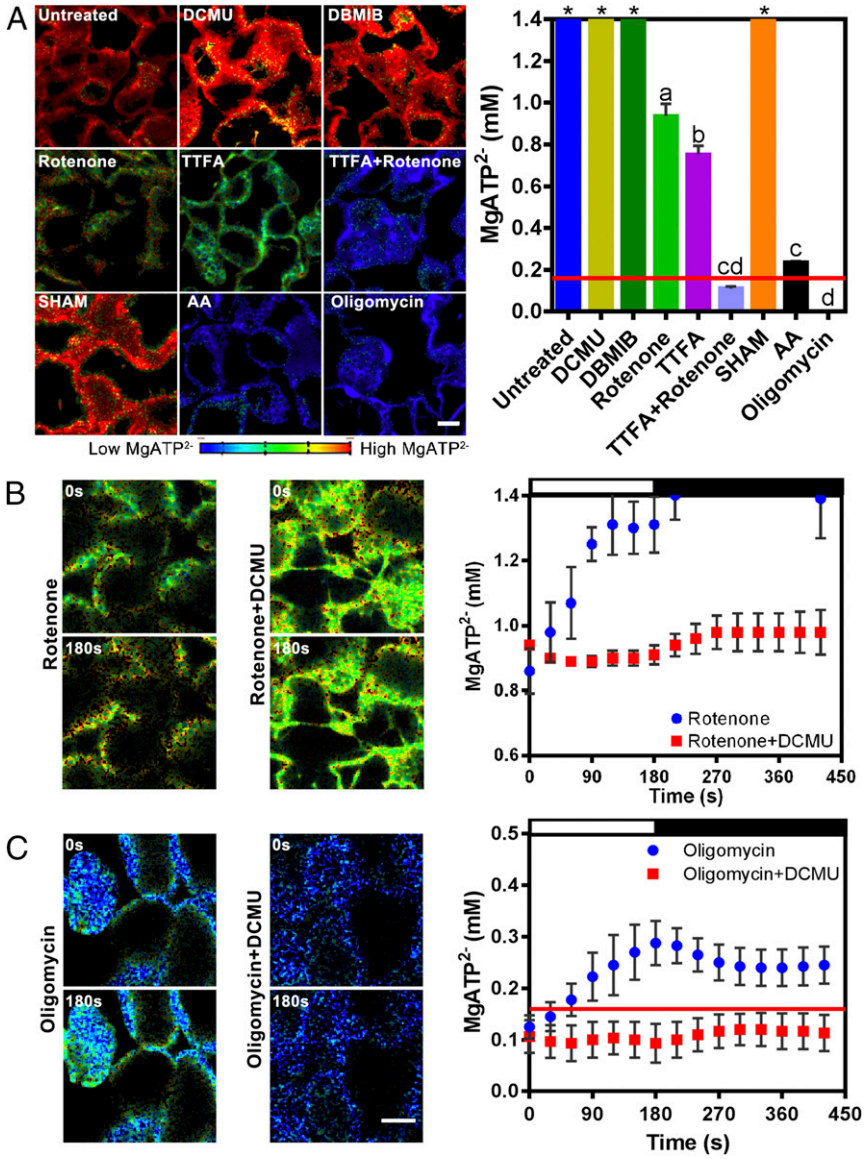

Fig. 4. Contribution of mitochondrion to cytosolic $MgATP^{2-}$ concentration. (*A*) Apparent cytosolic $MgATP^{2-}$ concentrations in cotyledon cells of 10-d-old *Arabidopsis* seedlings in darkness assessed by stably expressed AT1.03-nD/nA. The means (±SEM) of eight plants are shown in the bar chart. Groups with significant difference by one-way ANOVA with post hoc Tukey HSD test ($P < 0.05$) are indicated by different letters. The maximal $MgATP^{2-}$ that can be reported by AT1.03-nD/nA is 1.4 mM. The groups marked by asterisks are significantly different from the groups marked by letters, but whether they have intergroup differences is not known. [Scale bar (all panels): 20 μm.] The red line indicates the lower detection limit of AT1.03-nD/nA (0.16 mM). (*B* and *C*) The change of cytosolic $MgATP^{2-}$ concentration in illuminated (296 $\mu mol \cdot m^{-2} \cdot s^{-1}$) cotyledon ($n = 3$; mean ± SEM). The black and white bars indicate dark and illumination period, respectively. [Scale bar (all panels): 20 μm.] The red line indicates the lower detection limit of AT1.03-nD/nA (0.16 mM).

adequate to run photosynthesis without major defects under the experimental conditions (294 $\mu mol \cdot m^{-2} \cdot s^{-1}$). When complex II was inhibited by TTFA, $MgATP^{2-}$ concentration increased in the chloroplasts (0.33 ± 0.04 mM). Antimycin A lowered the changes in apparent $MgATP^{2-}$ concentration in chloroplasts upon illumination (0.08 ± 0.04 mM with antimycin A compared with 0.16 ± 0.03 mM in the untreated group). In antimycin A-treated seedlings, the lower oxygen evolution rate (*SI Appendix*, Fig. S7) and ETR were associated with a higher degree of nonphotochemical quenching (NPQ) (Fig. 5*B*), implying that the photosynthetic ETC was affected when the mitochondrial complex III was inhibited. An alternative explanation may be the direct inhibition of CEF by antimycin A (24), but cyanide (an alternative inhibitor of cytochrome *c*-dependent respiration) showed consistent effects (*SI Appendix*, Fig. S6). When the KCN-treated plants were subjected to a second light period, the increase in ATP was significantly lower than in the first light period (*SI Appendix*, Fig. S8*A*). Chlorophyll fluorescence analysis showed that the quantum yield [Y(II)] of KCN-treated plants was strongly affected (*SI Appendix*, Fig. S8*B*), suggesting that mitochondria in the KCN-treated plant cells were unable to dissipate excess reducing equivalents generated during photosynthesis. As a consequence, the photosynthetic ETC would be expected to be photoinhibited, compromising ATP synthesis in the chloroplasts. SHAM treatment lowered the changes in chloroplast $MgATP^{2-}$ (0.09 ± 0.03 mM) upon illumination. Similar to the impact of antimycin A, relatively low ETR and high NPQ values were detected in SHAM-treated seedlings (Fig. 5*B*). The oxygen evolution rate was also affected (*SI Appendix*, Fig. S7). SHAM inhibits both AOX and plastid oxidase (PTOX), which have been suggested to act as safety valves for

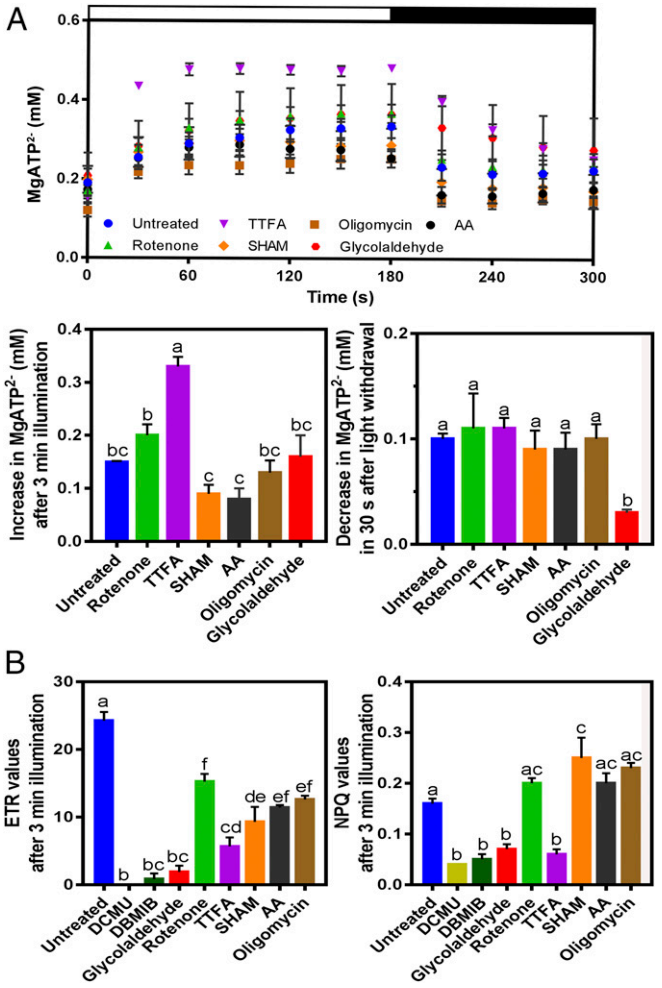

Fig. 5. Impact of mitochondrial activities on chloroplast performance. (*A*) Impact of inhibitors on stromal $MgATP^{2-}$ production (AT1.03-nD/nA) in cotyledon of 10-d-old plants. The black and white bars indicate dark and illumination (296 $\mu mol \cdot m^{-2} \cdot s^{-1}$) periods, respectively. The bars show the changes in stromal $MgATP^{2-}$ after illumination or withdrawal of light (n = 6 plants; mean ± SEM). Groups with significant difference by one-way ANOVA with post hoc Tukey HSD test ($P < 0.05$) are indicated by different letters. (*B*) Impact of inhibitors on chlorophyll fluorescence parameters. ETR and NPQ values were determined after 3 min of illumination (296 $\mu mol \cdot m^{-2} \cdot s^{-1}$) on the seedlings ($n$ = 6 plants; mean ± SEM). Groups with significant difference by one-way ANOVA with post hoc Tukey HSD test ($P < 0.05$) are indicated by different letters.

dissipating excess electrons in mitochondria and chloroplasts, respectively (25–27). Taken together, these data suggest that AOX and/or PTOX were required to dissipate excess electrons during illumination.

Discussion

The Expression Level of NTTs Affects the Level of Stromal ATP. ATP transport across the chloroplast envelope in mature photosynthetic cells was undetectable by our methods despite a steep concentration gradient between cytosol and stroma (Figs. 1 and 2). The direct import of ATP across the inner membrane requires a NTT, which mediates the electroneutral exchange of ATP^{4-} for ADP^{3-} + $H_2PO_4^-$ (28). Promoter-GUS staining showed that the *AtNTT2* promoter was highly active in cotyledons of 2- and 3-d-old seedlings, but its expression was not observed in hypocotyls or the cotyledons of 6-d-old seedlings or source leaves (22). We observed that while cytosolic FRET ratios in hypocotyls and cotyledons were steady in 3-, 4-, and 6-d-old seedlings, plastidic FRET ratios dropped gradually (Fig. 1*B*). Overexpression of AtNTTs in protoplasts led to lower cytosolic FRET ratios (Fig. 1*C*), which suggests transport of cytosolic ATP into chloroplasts via the NTTs. We did not observe a corresponding increase in stromal FRET ratios, suggesting that the imported ATP was consumed during the overnight incubation. Hence, the cytosolic ATP level is maintained by the down-regulation of AtNTTs in leaves. In young seedlings, when photosynthetic organelles are being developed, ATP is mainly supplied by the mobilization of reserves in the cotyledons by mitochondria. A high density of NTTs in the plastid inner membrane may allow cytosolic ATP to enter plastids efficiently to provide energy for chloroplast biogenesis, development, and/or lipid synthesis (Fig. 2). ATP import may become less relevant once the chloroplasts have fully established their photosynthetic function, at which time the entry of ATP from the cytosol into plastids appears restricted by the down-regulation of NTTs (22).

Reasons for Higher $MgATP^{2-}$ Concentrations in the Cytosol than in the Plastid Stroma. Cytosolic $MgATP^{2-}$ concentrations remained at high levels so long as mitochondrial ATP supply was secured (Fig. 4*A*). ATP generated in the mitochondria is exported to the cytosol via the active ATP/ADP carrier (AAC), which is the most abundant protein in the inner membrane of mitochondria (29). In contrast, $MgATP^{2-}$ concentrations in the chloroplast stroma of 10-d-old cotyledons remained at low levels with and without inhibitor treatment (*SI Appendix*, Fig. S9), supporting the idea that cytosolic ATP in photosynthetically active cells does not enter chloroplasts efficiently, or that the import rate is substantially slower than the ATP consumption rate in chloroplasts in the dark. Low $MgATP^{2-}$ levels in chloroplasts could reflect a continued energy demand for organellar activities in darkness, including RNA transcription, protein translation (30), and protein import (31). In the light, both ATP production and consumption would be far greater. The rapid rate of energy consumption of chloroplasts in the light is reflected in Fig. 5*A*. When illumination was halted, the apparent stromal $MgATP^{2-}$ level decreased rapidly (0.10 ± 0.02 mM in 30 s). In barley protoplasts, chloroplastic ATP levels also decreased sharply during the first second in darkness (10). A slower decrease was observed in glycolaldehyde-treated seedlings (0.03 ± 0.01 mM in 30 s). This result implied that the CBB cycle consumes a significant amount of ATP. This interpretation is also supported by early data from Bassham et al. (32), who showed that in *Scenedesmus* RuBP levels rapidly decreased in the dark whereas PGA increased, indicating that carboxylation continued for up to 30 s while further conversion of PGA in the CBB cycle was quickly stopped due to shortage of ATP (32). Hence, the high $MgATP^{2-}$ consumption activity in chloroplasts likely results in a low stromal $MgATP^{2-}$ level.

Since cytosolic ATP does not enter mature chloroplasts efficiently, chloroplasts have to generate ATP by endogenous phosphorylation and store its energy in the form of sugars and starch during the daytime, and then regenerate ATP through starch breakdown and glycolysis at night. The apparent stromal $MgATP^{2-}$ concentration (0.21 ± 0.08 mM) in the dark is a balance of ATP production (e.g., glycolysis) and ATP consumption. In dark, 0.25 mM ATP is enough for optimal translation of D1 protein in lysed chloroplasts and higher concentrations of ATP (0.5–25 mM) did not further increase the rate of translation. Without addition of exogenous ATP, D1 translation in lysed chloroplasts was significantly higher in light than in dark. Addition of exogenous ATP at 0.25–0.5 mM, but not at 0.05 mM, can further enhance D1 translation rate under illumination (20). Hence the apparent stromal $MgATP^{2-}$ concentrations in dark and in light determined here are in line with previous studies.

Export of Excess Reducing Equivalents Rather than Import of ATP Balances the NADPH/ATP Demand of the CBB Cycle in the Chloroplast. Unlike diatoms, in which mitochondria provide extra ATP to chloroplasts during periods of illumination to meet the ATP demand for carbon fixation (5), our data using *Arabidopsis thaliana* showed that cytosolic ATP does not enter chloroplasts of photosynthetically active tissues efficiently. While ATP production by the LEF appears to be insufficient (ATP:NADPH = 1.28) for carbon fixation (ATP: NADPH = 1.5), NADPH production by LEF (NADPH:ATP = 0.78) is present as a surplus (NADPH: ATP = 0.67). Excess NADPH in chloroplasts could reduce the photosystems and thereby cause photoinhibition and the production of reactive oxygen species (ROS) (33). Since ATP does not enter chloroplast efficiently (Fig. 2), ATP:NADPH can be balanced by extra ATP generation via CEF and by exporting excess NADPH. Unlike LEF, CEF produces ATP without generating reducing equivalents (3). Efficient export of reducing equivalents from the chloroplasts can also reduce the production of ROS and replenish $NADP^+$ for the LEF. Reducing equivalents from LEF can be exported from the chloroplasts via several pathways, including the malate-oxaloacetate (OAA) shuttle and the dihydroxyacetone phosphate (DHAP) shuttle (34). The export of reducing equivalents from the chloroplast in the form of malate is important (35) because excessive stromal reduction and lower photorespiration activity were observed in a T-DNA insertional mutant of the chloroplast malate transporter, *AtpOMT* (36). Under photorespiratory conditions, malate exported from chloroplasts can also indirectly contribute to mitochondrial ETC by supplying NADH for the peroxisomal conversion of hydroxypyruvate to glycerate, thereby making NADH from glycine oxidation available for mitochondrial ATP production (10). Indeed, under many conditions, mitochondria are the main supplier of ATP for the cytosol (37). Without the normal function of mitochondria in dissipating reducing equivalents, the ETR in chloroplasts was decreased during photosynthesis, implying that the chloroplast was affected when the mitochondrion was not able to transfer the reducing equivalents from the chloroplast to oxygen (Fig. 5*B*) (38, 39). Hence, the excess reducing power generated from chloroplasts can directly or indirectly fuel ATP production in the mitochondrion, which then supplies ATP to the cytosol and other cell compartments to fuel energy-demanding processes including sucrose synthesis, gene expression, and transport.

Materials and Methods

FRET ATP Sensor. The ATP sensor AT1.03-nD/nA consists of an $MgATP^{2-}$-binding epsilon-subunit of the *Bacillus subtilis* F_oF_1-ATP synthase linked between mseCFP (a variant of CFP) and a circularly permuted (cp173) monomeric Venus (a variant of YFP) (11). FRET occurs when the acceptor fluorescent protein (cp173Venus) is excited by the emission energy from the donor fluorescent protein (mseCFP). A change in the FRET signal reflects a change in $MgATP^{2-}$ concentration, and this is reported via ratiometric analysis, that is, FRET-derived acceptor emission/donor fluorophore (mseCFP) emission. This ratiometric method is insensitive to differences in sensor protein concentrations. To exclude emission contributed from sources other than FRET, correction coefficients for bleedthrough and cross-excitation were determined separately in different plant compartments (18, 40). The binding of AT1.03-nD/nA to $MgATP^{2-}$ is insensitive to pH changes between pH 7.3 and 8.5 (13). A related FRET-based sensor, cpFLIPPi-null, was used as a negative control in this study (18). Like AT1.03-nD/nA, cpFLIPPi-null contains mseCFP (FRET donor) and circularly permuted Venus (FRET acceptor), but it is not responsive to $MgATP^{2-}$.

pH Sensor. The pH-dependent fluorescent protein, circularly permuted YFP (cpYFP), was expressed in the mitochondrial matrix (41). cpYFP has a bimodal absorption spectrum with two peak maxima at 395 and 475 nm and a single emission peak at 528 nm (41). The absorption intensity of these two spectra is dependent on whether the chromophore of cpYFP is protonated or deprotonated. Briefly, protonated cpYFP displays a higher absorption around 395 nm and emits a higher signal at 528 nm if excited at 395 nm. cpYFP was shown to respond to pH (42), making it suitable for estimating the pH gradient resulting from the mitochondrial ETC activity under the assumption of stable cytosolic pH.

Plasmid Construct. cDNA encoding AT1.03-nD/nA was PCR-amplified from a pRSET vector that was purchased from Addgene using a forward primer (5′-ATTAGGATCCTCGAGTATGGTGAGCAAGGGC) and a reverse primer (5′-TCCGTCTAGATTACTCGATGTTGTGGCGGATCT). The amplified gene was cloned into the BamHI/XbaI sites of a modified Gateway pENTR vector (Invitrogen) with or without the *Nicotiana tabacum* chloroplast transketolase transit peptide (TKTP) (13). The gene cassettes were transferred into the pEarleyGate100 vector using gateway LR clonase (Invitrogen) (43). In pEarleyGate100, the transcription of sensor cDNAs was driven by a 35S-promoter for constitutive expression in the plant system. Constructs were verified by nucleotide sequencing. Plant expression vector for cpYFP expression in the mitochondrial matrix (pH2GW7:mt-cpYFP) was described previously (42).

The coding sequences of AtNTT1 (At1g80300) and AtNTT2 (At1g15500) were amplified from the leaf cDNA of 20-d-old wild-type (WT) *Arabidopsis thaliana* using specific primers (ATNTT1-BamHI-F, TAATGGATCCATGGAAGCTGTGATTCAAAC; ATNTT1-XbaI-R, GCCATCTAGATTATAAGTTGGTGGGAGCAG; ATNTT2-BamHI-F, TAATGGATCCATGGAAGGTCTGATTCAAAC; ATNTT2-XbaI-R, CGTCTCTAGACTAAATGCCAGTAGGAGTAGAT) by *Pfx* polymerase (Invitrogen). The PCR products were cloned into the pENTR/D-TOPO vector (Thermo Fisher Scientific) under the control of a CaMV 35S promoter. The plasmids were isolated using QIAGEN Plasmid Maxi kit (Qiagen) for protoplast transformation.

Plant Transformation and Growth Conditions. WT *Arabidopsis thaliana* plants (ecotype Columbia, Col-0) were used in this study. The pEarleyGate100 and pH2GW7 constructs were transformed into the *Arabidopsis* plants using *Agrobacterium tumefaciens* (strain GV3101). Positive transformants were screened using a fluorescence microscope (Nikon Eclipse 80i), and T3 plants were used for imaging. The WT and transformed plants were germinated and grown on Murashige and Skoog plates supplemented with 2% (wt/vol) sucrose under a 16-h light/8-h dark regime with a light intensity of 120–150 $\mu mol \cdot m^{-2} \cdot s^{-1}$.

Confocal Laser-Scanning Microscopy Imaging. Fluorescent images were obtained under a Zeiss LSM710/780 confocal microscope (Carl Zeiss Microscopy). Imaging was performed with a 40× and 63× oil-immersion lens in multitrack mode with line switching. cpYFP was excited at 488 (I_{488}) and 405 nm (I_{405}), and the emission signals were detected at 505–530 nm. AT1.03-nD/nA was excited at 458 nm at 7.5%, 10%, and 15% of maximal power for protoplasts, seedlings, and chloroplasts, respectively, and the emission signals were detected at 470–507 nm ($Em_{470–507}$, mseCFP image) and 526–545 nm ($Em_{526–545}$, FRET image). AT1.03-nD/nA was also excited at 515 nm (0.18% of maximal power for all samples) to directly excite Venus and detected at 526–545 nm (cp173Venus image). Chlorophyll fluorescence was detected at 629–700 nm. SYTOX orange nucleic acid stain was excited at 543 nm (1% of maximal power), and the emission signals were detected at 565–604 nm. White light illumination was achieved using a halogen lamp (HAL 100 W; Philips) attached to the confocal system.

Image Processing and Ratiometric FRET Analysis. The confocal laser-scanning microscopy (CLSM) images were imported into a custom MatLab (The MathWorks, https://www.mathworks.com/products/matlab.html) analysis suite (44). Ratio images were calculated on a pixel-by-pixel basis as Ex_{488}/Ex_{405} and $Em_{526–545}/Em_{470–507}$ for cpYFP and AT1.03-nD/nA, respectively. The images were analyzed by spatial averaging in (x, y) using a 3×3 kernel and subtraction of the background for each channel measured from the dark side of the images. Pixels with intensity values less than 2 SD units above the background or within 10% of the saturation were masked from the ratio image and excluded from all quantitative measurements. The quantitative measurements were calculated as the ratio of the mean intensity of each channel.

Correction coefficients for spectral bleedthrough (CFP emission detected in the Venus channel) and cross-excitation (Venus excited by CFP excitation wavelength) were applied to correct for the FRET emission intensity of AT1.03-nD/nA, yielding a sensitized FRET emission value (18). Bleedthrough and cross-excitation coefficients were determined from images of plants expressing single fluorescent proteins (mseCFP or cp173Venus) using the same image settings as those used for the experimental measurements (18). Linear regression was applied to calculate the fitted straight lines of FRET emission versus CFP (from plants expressing mseCFP only) and FRET emission versus Venus direct excitation (from plants expressing cp173Venus only). The slopes of the fitted straight lines were considered the bleedthrough

coefficient (coefficient a) and cross-excitation coefficient (coefficient b). Sensitized FRET was calculated by the following formula: Sensitized FRET = Raw FRET − (CFP emission*a) − (Venus emission*b) (18).

Location-Specific Spectral Correction Coefficients for FRET-Based AT1.03-nD/nA. To exclude the intensity contributed from sources other than the FRET signal, correction coefficients for bleedthrough and cross-excitation were determined separately in different plant compartments (18). CFP, direct Venus, and FRET images of the cytosol and plastids in cotyledon mesophyll, hypocotyl, and root epidermal cells were captured from at least eight individual plants expressing mseCFP or cp173Venus only (18). The slopes of the fitted straight line of FRET versus mseCFP or FRET versus direct Venus excitation were used as the bleedthrough and cross-excitation coefficients, respectively. In the cotyledon, the bleedthrough coefficients (coefficient a) in the cytosol and plastids were 0.2 and 0.36, respectively, whereas the cross-excitation coefficients (coefficient b) in the cytosol and plastids were 0.64 and 0.62 (*SI Appendix*, Fig. S3). In the root, the corresponding values were 0.22, 0.41, 0.69, and 0.79 (*SI Appendix*, Fig. S3). In the hypocotyl, the corresponding values were 0.24, 0.25, 0.41, and 0.53 (*SI Appendix*, Fig. S3). Different coefficients were observed in different compartments of the same tissue (e.g., cotyledon cytosol versus cotyledon plastid) and the same compartment in different tissues (e.g., cotyledon plastid versus root plastid). The coefficients were used to calculate the sensitized FRET as follows:

Because Sensitized FRET = RAW FRET − (CFP emission*a) − (Venus emission*b),

In the cotyledon cytosol, Sensitized FRET = Raw FRET − CFP emission*0.2 − Venus emission*0.64.

In the cotyledon plastid, Sensitized FRET = Raw FRET − CFP emission*0.36 − Venus emission*0.62.

In hypocotyl cytosol, Sensitized FRET = Raw FRET − CFP emission*0.24 − Venus emission*0.41.

In hypocotyl plastid, Sensitized FRET = Raw FRET − CFP emission*0.25 − Venus emission*0.53.

In the root cytosol, Sensitized FRET = Raw FRET − CFP emission*0.22 − Venus emission*0.69.

In the root plastid, Sensitized FRET = Raw FRET − CFP emission*0.41 − Venus emission*0.79.

Calibration of Sensitized FRET Ratios to $MgATP^{2-}$ Concentrations. AT1.03-nD/nA, mseCFP, and cp173Venus fluorescent proteins were expressed in *Escherichia coli* and purified with His-affinity chromatography from cell lysates as previously described (18). The pRSET AT1.03-nD/nA vector was introduced into *E. coli* strain BL21, and a single colony was cultured in 100 mL of LB medium with ampicillin overnight at 25 °C. The cells were harvested by centrifugation (5,000 × *g*, 10 min) and then lysed with lysis buffer [300 mM NaCl, 20 mM Tris·HCl (pH 7.5), 10 mM imidazole, 1% (vol/vol) protease inhibitor mixture] and ruptured by sonication (~30 s with 50% output) on ice. The expressed AT1.03-nD/nA protein was purified from the cell lysates using His-affinity chromatography with elution in 100 mM Na-phosphate (pH 8.0), 200 mM NaCl, and 400 mM imidazole. The eluents were dialyzed against 20 mM Tris·HCl (pH 7.5), 150 mM NaCl overnight at 4 °C. The purified proteins were quantified using the Bradford assay.

To estimate $MgATP^{2-}$ concentrations in vivo, sensitized FRET/CFP ratios of the purified recombinant sensor (6 μM) were calibrated with increasing $MgATP^{2-}$ concentrations (0–6 mM; equimolar concentrations of ATP and $MgCl_2$) in a buffer containing 50 mM Mops-KOH, pH 7.3, 50 mM KCl, 0.5 mM $MgCl_2$, and 0.05% (vol/vol) Triton X-100 under the same image acquisition settings used for in vivo measurements (*SI Appendix*, Fig. S2). The bleedthrough coefficient and cross-excitation coefficient were determined using mseCFP and cp173Venus fluorescent proteins, respectively. For AT1.03-nD/nA, the sensitized FRET ratio without the ligand (0 mM $MgATP^{2-}$) was 0.39, which increased steadily to 1.38 at the $MgATP^{2-}$ concentration of 1.4 mM. The sensitized FRET ratio was relatively stable beyond the $MgATP^{2-}$ concentration of 1.4 mM. The observed sensitized FRET ratio data were fit to the following single-site binding equation: $R - R_0 = ((R_{max} - R_0)*L^n)/(K_d^n + L^n)$, where R is the FRET ratio, R_0 is the ratio with no ligand, R_{max} is the ratio at saturation, L is the ligand (ATP) concentration, K_d is the disassociation constant, and n is Hill's coefficient (*SI Appendix*, Fig. S2) (45). Based on the calibrated curves, K_d for $MgATP^{2-}$ of AT1.03-nD/nA at 22 °C was 0.627 mM. Assuming K_d and n are constant under in vitro and in vivo conditions, by substituting R_0 and R_{max} with the minimum (0.27) and maximum (1.6) FRET ratios measured in vivo, respectively, we obtain the following conversion equation of the FRET ratio to the apparent $MgATP^{2-}$ concentration in vivo: $R - 0.27 = ((1.6 - 0.27))*L^{1.675})/(0.627^{1.675} + L^{1.675})$ (*SI Appendix*, Fig. S2). The effective range of the sensor was estimated between K_d*0.25 to K_d*4 (45). Hence, the effective range of AT1.03-nD/nA was at least 0.16 mM and 2.51 mM at maximum (*SI Appendix*, Fig. S2). The FRET ratio in the subsequent measurement involving AT1.03-nD/nA of 10-d-old seedlings was converted to the ATP concentration using the aforementioned equation. As a conservative approach, we assumed that the detection limit measured in the in vitro calibration (1.4 mM) was also the saturation point in vivo.

Inhibitor Treatment. Inhibitors used in these studies include the following: inhibitor of the photosynthetic chain (20 μM DCMU and 10 μM DBMIB), CBB cycle (20 mM glycolaldehyde), mitochondrial complex I (50 μM rotenone), mitochondrial complex II (100 μM TTFA), mitochondrial AOX (2 mM SHAM), mitochondrial complex III (10 μM antimycin A), and mitochondrial ATP synthase (10 μM oligomycin A). For inhibitor treatments, seedlings were immersed in medium supplemented with or without the inhibitors and vacuum-infiltrated for 5 min. Unless otherwise stated, the treated seedlings were incubated in the dark for 1 h before imaging or other measurement.

To confirm that the effects of the inhibitors were specific to the ETC and did not result from unfavorable side effects, the viability of plant cells was examined by SYTOX orange (Thermo Fisher Scientific), which is a fluorescent nucleic acid stain that selectively penetrates nonviable cells (46). We applied 25 nM stain to the seedlings after inhibitor treatments. A distinct emission signal from SYTOX orange was not detected in any of the treated seedlings, indicating that the treatment method did not severely affect the viability of the plant cells (*SI Appendix*, Fig. S10). SYTOX orange was also used to assess chloroplast integrity. Chloroplasts isolated from 5- and 10-d-old seedlings were incubated with 25 nM SYTOX orange for 10 min. After removal of excess stain, chloroplasts were resuspended in a buffer containing 5 mM $MgCl_2$ with 5 mM ATP before imaging (Fig. 2*B*).

Oxygen Consumption and Evolution Measurement. Respiratory oxygen consumption and photosynthetic oxygen evolution rate were measured with a Clark-type electrode (Hansatech). Measurements were performed using 0.05 g of 10-d-old seedlings. Oxygen was measured in the dark for 3 min before illuminating the seedlings at an intensity of 280 $\mu mol \cdot m^{-2} \cdot s^{-1}$ for 3 min. Light was withdrawn, and the oxygen level was measured in the dark again for 3 min. The consumption or evolution rate was determined for each minute interval. The oxygen levels from the fourth to fifth and seventh to eighth minutes were used to calculate the evolution rate and consumption rate (nanomoles of O_2 per second), respectively. The rate of photosynthesis was calculated as the evolution rate minus consumption rate.

Chlorophyll Fluorescence Measurements. Chlorophyll fluorescence in 10-d-old seedlings was monitored with the IMAGING-PAM M-Series Maxi Version (WALZ). Before the measurement, the treated seedlings were incubated in the dark for 1 h. After the maximum and initial fluorescence (Fm Fo) were determined and a delay of 40 s, the plants were illuminated with a light intensity of 296 $\mu mol \cdot m^{-2} \cdot s^{-1}$ for 3 min. A saturation pulse was applied at the end of the 3-min illumination to measure the chlorophyll fluorescence parameters.

Protoplast Isolation and Transfection. Mesophyll protoplasts were isolated from 4-wk-old leaves of *Arabidopsis* plants expressing C-AT1.03-nD/nA or TKTP-AT1.03-nD/nA by the tape–*Arabidopsis* sandwich method (47). Leaves were fixed on tape with the lower epidermal surface facing upward and peeled with a strip of tape. The exposed mesophyll cells were digested in digestion buffer containing 20 mM 2-(*N*-morpholino)ethanesulfonic acid (Mes) buffer (pH 5.7) containing 1% (wt/vol) cellulose (Yakult), 0.25% (wt/vol) macerozyme (Yakult), 10 mM $CaCl_2$, 20 mM KCl, 0.1% (wt/vol) BSA, and 0.4 M mannitol with gentle agitation (50 rpm) for 1 h. After washing the released protoplasts with W5 solution (2 mM Mes, pH 5.7, 154 mM NaCl, 125 mM $CaCl_2$, and 5 mM KCl) twice, protoplasts were incubated on ice for 30 min, centrifuged, and resuspended into MMg solution (4 mM Mes, pH 5.7, 15 mM $MgCl_2$, and 0.4 M mannitol). Protoplasts were transfected with plasmids by incubating for 10 min at room temperature in the presence of 20% (wt/vol) PEG4000 with 0.1 M $CaCl_2$ and 0.2 M mannitol. After washing with W5 solution twice, transfected protoplasts were incubated in 1 mL of WI solution [0.5 M mannitol, 4 mM Mes (pH 5.7), and 20 mM KCl] in the dark at 25 °C overnight.

Chloroplast Isolation and Imaging. Chloroplasts were isolated from seedlings, cotyledon or leaves of plants expressing TKTP-AT1.03-nD/nA as previously described (48). After Percoll gradient centrifugation, the chloroplasts were

washed and resuspended in a buffer containing 300 mM sucrose, 50 mM Hepes-KOH (pH 7.5), 10 mM KCl, 10 mM NaCl, 5 mM $MgCl_2$, and 0.1% (wt/vol) BSA. The chloroplasts were incubated with 5 mM ATP for 5 min in room temperature before confocal imaging.

ACKNOWLEDGMENTS. We thank Marlene Elsässer (University of Bonn) for support with optimizing sensor imaging at dark–light transitions. This project was supported by the Seed Funding Program for Basic Research (201411159108), the Hong Kong Research Grants Council Area of Excellence Scheme (AoE/M-403/16), the Innovation and Technology Fund (Funding Support to Partner State Key Laboratories in Hong Kong) of the Hong Kong Special Administrative Region, China, and the US Department of Energy (DE-SC01014037). M.S. gratefully acknowledges funding by the Deutsche Forschungsgemeinschaft through the Emmy Noether Programme (SCHW1719/1-1), Research Training Group GRK 2064, and Grant SCHW1719/5-1 as part of the package PAK918.

1. Allen JF (2003) Cyclic, pseudocyclic and noncyclic photophosphorylation: New links in the chain. *Trends Plant Sci* 8:15–19.
2. Kramer DM, Evans JR (2011) The importance of energy balance in improving photosynthetic productivity. *Plant Physiol* 155:70–78.
3. Shikanai T (2016) Regulatory network of proton motive force: Contribution of cyclic electron transport around photosystem I. *Photosynth Res* 129:253–260.
4. Finazzi G, Johnson GN (2016) Cyclic electron flow: Facts and hypotheses. *Photosynth Res* 129:227–230.
5. Bailleul B, et al. (2015) Energetic coupling between plastids and mitochondria drives CO_2 assimilation in diatoms. *Nature* 524:366–369.
6. Heldt HW (1969) Adenine nucleotide translocation in spinach chloroplasts. *FEBS Lett* 5:11–14.
7. Cheung CY, Poolman MG, Fell DA, Ratcliffe RG, Sweetlove LJ (2014) A diel flux balance model captures interactions between light and dark metabolism during day-night cycles in C3 and crassulacean acid metabolism leaves. *Plant Physiol* 165:917–929.
8. Gardeström P, Igamberdiev AU, Raghavendra AS (2002) Mitochondrial functions in the light and significance to carbon-nitrogen interactions. *Photosynthetic Nitrogen Assimilation and Associated Carbon and Respiratory Metabolism*, eds Foyer CH, Noctor G (Kluwer Academic Publishers, Dordrecht, The Netherlands), pp 151–172.
9. Gardeström P (1987) Adenylate ratios in the cytosol, chloroplasts and mitochondria of barley leaf protoplasts during photosynthesis at different carbon-dioxide concentrations. *FEBS Lett* 212:114–118.
10. Gardeström P, Wigge B (1988) Influence of photorespiration on ATP/ADP ratios in the chloroplasts, mitochondria, and cytosol, studied by rapid fractionation of barley (*Hordeum vulgare*) protoplasts. *Plant Physiol* 88:69–76.
11. Imamura H, et al. (2009) Visualization of ATP levels inside single living cells with fluorescence resonance energy transfer-based genetically encoded indicators. *Proc Natl Acad Sci USA* 106:15651–15656.
12. Hatsugai N, Perez Koldenkova V, Imamura H, Noji H, Nagai T (2012) Changes in cytosolic ATP levels and intracellular morphology during bacteria-induced hypersensitive cell death as revealed by real-time fluorescence microscopy imaging. *Plant Cell Physiol* 53:1768–1775.
13. De Col V, et al. (2017) ATP sensing in living plant cells reveals tissue gradients and stress dynamics of energy physiology. *eLife* 6:e26770.
14. Tsuyama T, et al. (2013) In vivo fluorescent adenosine 5′-triphosphate (ATP) imaging of *Drosophila melanogaster* and *Caenorhabditis elegans* by using a genetically encoded fluorescent ATP biosensor optimized for low temperatures. *Anal Chem* 85:7889–7896.
15. Gupta RK, Gupta P, Yushok WD, Rose ZB (1983) Measurement of the dissociation constant of MgATP at physiological nucleotide levels by a combination of ^{31}P NMR and optical absorbance spectroscopy. *Biochem Biophys Res Commun* 117:210–216.
16. Portis AR (1981) Evidence of a low stromal Mg^{2+} concentration in intact chloroplasts in the dark: I. Studies with the ionophore A23187. *Plant Physiol* 67:985–989.
17. Krause GH (1977) Light-induced movement of magnesium ions in intact chloroplasts. Spectroscopic determination with eriochrome blue SE. *Biochim Biophys Acta* 460:500–510.
18. Banerjee S, Garcia LR, Versaw WK (2016) Quantitative imaging of FRET-based biosensors for cell- and organelle-specific analyses in plants. *Microsc Microanal* 22:300–310.
19. Gout E, Rébeillé F, Douce R, Bligny R (2014) Interplay of Mg^{2+}, ADP, and ATP in the cytosol and mitochondria: Unravelling the role of Mg^{2+} in cell respiration. *Proc Natl Acad Sci USA* 111:E4560–E4567.
20. Edhofer I, Muhlbauer SK, Eichacker LA (1998) Light regulates the rate of translation elongation of chloroplast reaction center protein D1. *Eur J Biochem* 257:78–84.
21. Reinhold T, et al. (2007) Limitation of nocturnal import of ATP into *Arabidopsis* chloroplasts leads to photooxidative damage. *Plant J* 50:293–304.
22. Reiser J, Linka N, Lemke L, Jeblick W, Neuhaus HE (2004) Molecular physiological analysis of the two plastidic ATP/ADP transporters from *Arabidopsis*. *Plant Physiol* 136:3524–3536.
23. Møller IM, Rasmusson AG, Fredlund KM (1993) NAD(P)H-ubiquinone oxidoreductases in plant mitochondria. *J Bioenerg Biomembr* 25:377–384.
24. Labs M, Rühle T, Leister D (2016) The antimycin A-sensitive pathway of cyclic electron flow: From 1963 to 2015. *Photosynth Res* 129:231–238.
25. Yoshida K, Watanabe C, Kato Y, Sakamoto W, Noguchi K (2008) Influence of chloroplastic photo-oxidative stress on mitochondrial alternative oxidase capacity and respiratory properties: A case study with *Arabidopsis* yellow variegated 2. *Plant Cell Physiol* 49:592–603.
26. Yoshida K, Terashima I, Noguchi K (2007) Up-regulation of mitochondrial alternative oxidase concomitant with chloroplast over-reduction by excess light. *Plant Cell Physiol* 48:606–614.
27. Atteia A, et al. (2004) Identification of prokaryotic homologues indicates an endosymbiotic origin for the alternative oxidases of mitochondria (AOX) and chloroplasts (PTOX). *Gene* 330:143–148.
28. Trentmann O, Jung B, Neuhaus HE, Haferkamp I (2008) Nonmitochondrial ATP/ADP transporters accept phosphate as third substrate. *J Biol Chem* 283:36486–36493.
29. Klingenberg M (2008) The ADP and ATP transport in mitochondria and its carrier. *Biochim Biophys Acta* 1778:1978–2021.
30. Sun Y, Zerges W (2015) Translational regulation in chloroplasts for development and homeostasis. *Biochim Biophys Acta* 1847:809–820.
31. Shi LX, Theg SM (2013) Energetic cost of protein import across the envelope membranes of chloroplasts. *Proc Natl Acad Sci USA* 110:930–935.
32. Bassham JA, Shibata K, Steenberg K, Bourdon J, Calvin M (1956) The photosynthetic cycle and respiration: Light-dark transients. *J Am Chem Soc* 78:4120–4124.
33. Pospísil P (2009) Production of reactive oxygen species by photosystem II. *Biochim Biophys Acta* 1787:1151–1160.
34. Heineke D, et al. (1991) Redox transfer across the inner chloroplast envelope membrane. *Plant Physiol* 95:1131–1137.
35. Scheibe R (2004) Malate valves to balance cellular energy supply. *Physiol Plant* 120:21–26.
36. Kinoshita H, et al. (2011) The chloroplastic 2-oxoglutarate/malate transporter has dual function as the malate valve and in carbon/nitrogen metabolism. *Plant J* 65:15–26.
37. Gardeström P, Igamberdiev AU (2016) The origin of cytosolic ATP in photosynthetic cells. *Physiol Plant* 157:367–379.
38. Vishwakarma A, Tetali SD, Selinski J, Scheibe R, Padmasree K (2015) Importance of the alternative oxidase (AOX) pathway in regulating cellular redox and ROS homeostasis to optimize photosynthesis during restriction of the cytochrome oxidase pathway in *Arabidopsis thaliana*. *Ann Bot* 116:555–569.
39. Krömer S, Heldt HW (1991) On the role of mitochondrial oxidative-phosphorylation in photosynthesis metabolism as studied by the effect of oligomycin on photosynthesis in protoplasts and leaves of barley (*Hordeum vulgare*). *Plant Physiol* 95:1270–1276.
40. Broussard JA, Rappaz B, Webb DJ, Brown CM (2013) Fluorescence resonance energy transfer microscopy as demonstrated by measuring the activation of the serine/threonine kinase Akt. *Nat Protoc* 8:265–281.
41. Nagai T, Sawano A, Park ES, Miyawaki A (2001) Circularly permuted green fluorescent proteins engineered to sense Ca^{2+}. *Proc Natl Acad Sci USA* 98:3197–3202.
42. Schwarzländer M, Logan DC, Fricker MD, Sweetlove LJ (2011) The circularly permuted yellow fluorescent protein cpYFP that has been used as a superoxide probe is highly responsive to pH but not superoxide in mitochondria: Implications for the existence of superoxide "flashes." *Biochem J* 437:381–387.
43. Earley KW, et al. (2006) Gateway-compatible vectors for plant functional genomics and proteomics. *Plant J* 45:616–629.
44. Fricker MD (2016) Quantitative redox imaging software. *Antioxid Redox Signal* 24:752–762.
45. Banerjee S, Versaw WK, Garcia LR (2015) Imaging cellular inorganic phosphate in *Caenorhabditis elegans* using a genetically encoded FRET-based biosensor. *PLoS One* 10:e0141128.
46. Truernit E, Haseloff J (2008) A simple way to identify non-viable cells within living plant tissue using confocal microscopy. *Plant Methods* 4:15.
47. Wu FH, et al. (2009) Tape-*Arabidopsis* sandwich—a simpler *Arabidopsis* protoplast isolation method. *Plant Methods* 5:16.
48. Zhang R, et al. (2016) AtPAP2 modulates the import of the small subunit of Rubisco into chloroplasts. *Plant Signal Behav* 11:e1239687.